ELSEVIER

Reconciling strong slab pull and weak plate bending: The plate motion constraint on the strength of mantle slabs

Benjun Wu [a], Clinton P. Conrad [b],*, Arnauld Heuret [c,1], Carolina Lithgow-Bertelloni [d], Serge Lallemand [e]

[a] Department of Earth and Planetary Sciences, Johns Hopkins University, Baltimore, MD 21218, USA
[b] Department of Geology and Geophysics, University of Hawaii at Manoa, Honolulu, HI 96822, USA
[c] Dipartimento Scienze Geologiche, Università Roma TRE, Roma, Italy
[d] Department of Earth Sciences, University College London, London, WC1E6BT, UK
[e] Laboratoire Géosciences Montpellier, Université Montpellier 2, CNRS, France

ARTICLE INFO

ABSTRACT

Although subducting slabs undergo a bending deformation that resists tectonic plate motions, the magnitude of this resistance is not known because of poor constraints on slab strength. However, because slab bending slows the relatively rapid motions of oceanic plates, observed plate motions constrain the importance of bending. We estimated the slab pull force and the bending resistance globally for 207 subduction zone transects using new measurements of the bending curvature determined from slab seismicity. Predicting plate motions using a global mantle flow model, we constrain the viscosity of the bending slab to be at most ~300 times more viscous than the upper mantle; stronger slabs are intolerably slowed by the bending deformation. Weaker slabs, however, cannot transmit a pull force sufficient to explain rapid trenchward plate motions unless slabs stretch faster than seismically observed rates of ~10^{-15} s^{-1}. The constrained bending viscosity (~2×10^{23} Pa s) is larger than previous estimates that yielded similar or larger bending resistance (here ~25% of forces). This apparent discrepancy occurs because slabs bend more gently than previously thought, with an average radius of curvature of 390 km that permits subduction of strong slabs. This gentle bending may ultimately permit plate tectonics on Earth.

© 2008 Elsevier B.V. All rights reserved.

1. Introduction

Subduction of cold, dense, oceanic lithosphere into the mantle interior is fundamental to plate tectonics because it allows the entire thickness of the oceanic lithosphere to participate in convective mantle flow (e.g., Elsasser, 1969; Richter, 1977). However, the cold temperatures of the oceanic lithosphere also enhance its mechanical strength (Kohlstedt et al., 1995) and hinder the bending deformation that is necessary for plates to subduct (Billen and Hirth, 2007). Indeed, some authors (Conrad and Hager, 1999, 2001; Buffett, 2006; Buffett and Rowley, 2006) argued that plate bending at subduction zones may dissipate up to ~40% of the mantle's convective energy, making plate bending as important as mantle shear for determining plate tectonic rates (Faccenna et al., 2007). Experimental studies (Becker et al., 1999; Bellahsen et al., 2005) also indicate that plate bending can limit the rate of subduction, but only if plates both bend sharply and are highly

viscous. Here, we use a new global catalog of radius of curvature measurements for bending slabs around the world (Heuret, 2005) to constrain the slab effective rheology and thus the importance of bending resistance to global plate motions.

Significant controversy persists regarding the effective strength of bending slabs relative to the underlying mantle. Although the strong temperature-dependence of rock rheology should make cold slabs significantly stiffer than the surrounding mantle, plastic and/or brittle deformation may decrease their mechanical strength (e.g., Kohlstedt et al., 1995), making their net effective strength uncertain. Recently, subduction experiments in the laboratory have revealed that the range of observed upper mantle slab shapes require slabs to be 150–500 times stiffer than the surrounding mantle (Funiciello et al., in press). Some numerical studies using similar constraints require even larger slab viscosities (Billen and Hirth, 2007). On the other hand, geoid studies (Moresi and Gurnis, 1996; Zhong and Davies, 1999) suggest significantly lower viscosity contrasts and weaker slabs. Thus, although slabs are generally considered to be stronger than the surrounding mantle, the degree of strengthening is unknown to within at least an order of magnitude.

Because the bending resistance depends on the poorly constrained lithospheric viscosity, the importance of bending for plate motions remains uncertain. However, the bending resistance is also a strong

function of lithospheric thickness, which means that bending should preferentially resist subduction of thicker oceanic lithosphere. Buffett and Rowley (2006) showed that this effect strongly influences the direction of plate motions, and that the motions of the Pacific and Nazca plates are best fit if bending dissipates ~36% and ~14%, respectively, of the energy released by the descent of their attached upper mantle slabs. Faccenna et al. (2007), obtained similar results by considering the rates of subduction. However, neither study considered the effects of global mantle flow. By contrast, studies that do account for global mantle flow (e.g., Lithgow-Bertelloni and Richards, 1998; Becker and O'Connell, 2001; Conrad and Lithgow-Bertelloni, 2002, 2004; Becker, 2006) do not examine the effect of plate bending at subduction zones because it is difficult to simulate the detailed deformation within a subduction zone in global-scale models. In this study, we include a parameterization of the bending resistance (Buffett, 2006) within a global flow model, and in doing so place new constraints on the importance of bending to global tectonics.

2. Plate bending and the force balance on plates

The observed relative motions between plates can be predicted successfully when driven by "slab pull" from upper mantle slabs (F_{pull}, transmitted via guiding stresses) and "slab suction" from lower mantle slabs ($F_{suction}$, transmitted via flow-induced tractions on the base of plates), and resisted by viscous stresses in the mantle (F_{drag}, mantle drag) (e.g., Becker and O'Connell, 2001; Conrad and Lithgow-Bertelloni, 2002, 2004). By implementing a simple kinematic description of strain in the equations that govern the mechanical equilibrium of a thin viscous sheet, Buffett (2006) expressed the resistance to bending as a net horizontal force, $F_{bending}$, that acts on the subducting plate, but in a direction opposite to subduction. Thus, $F_{bending}$ subtracts from F_{pull} to produce a net driving force of $F_{suction} + F_{pull} - F_{bending}$ that is balanced by mantle drag force F_{drag} associated with the motion of each plate over the viscous mantle. The plate motions are thus sensitive to the plate bending resistance $F_{bending}$, and will be significantly slowed if $F_{bending}$ is a sizeable fraction of F_{pull}. Below we estimate these various driving forces, which we will later use to predict plate motions.

2.1. Slab pull force

The slab pull force is given by $F_{pull} = HD\Delta\rho g/\sqrt{\pi}$, where $H = 2\sqrt{\kappa A_S}$ is the thickness of the plate ($\kappa = 10^{-6}$ m²/s and A_S is the plate age at the time of subduction), D is the vertical extent of the slab in the upper mantle (670 km or less), $\Delta\rho = \rho\alpha\Delta T$ is the excess density of the plate relative to the surrounding mantle ($\rho = 3300$ kg/m³ is the density, $\alpha = 3 \times 10^{-5}$ K⁻¹ is the thermal expansivity, $\Delta T = 1200$ K is the lithospheric temperature drop), and g is the acceleration due to gravity (Conrad and Lithgow-Bertelloni, 2002). Using seafloor age maps and seismological databases to constrain slab properties, Lallemand et al. (2005) compiled estimates of A_S and D (along with several other properties) for 207 subduction zone profiles around the world (Table 1); we used these estimates to calculate F_{pull} acting on subducting plates (Fig. 1a). We omitted 14 of Lallemand et al.'s (2005) subduction zones because they were located between plates that are too small to include in this study. Flattening bathymetry for seafloor older than 80 Myr suggests that oceanic lithosphere may reach a maximum thickness of about 100 km at this age (e.g., Stein and Stein, 1992). For this reason, we used $H = 100$ km at subduction transects where $A_S > 80$ Myr. Several slabs have values of D smaller than 670 km (Table 1), which indicates that these slabs do not extend through the entire upper mantle. These "truncated" slabs typically result form recent initiation of subduction or a noticeably missing or detached lower slab, and not from shallow dip ("flat slab") situations, which (Lallemand et al., 2005) traced horizontally before measuring the slab's vertical extent (D).

2.2. Slab suction force

To compute the slab suction force, $F_{suction}$, we predict the instantaneous mantle flow driven by slabs (Lithgow-Bertelloni and Richards, 1998) in the lower mantle subject to a no slip surface boundary condition, using the propagator matrix solutions to the flow equations (Hager and O'Connell, 1981). Because upper mantle slabs drive slab pull (Conrad and Lithgow-Bertelloni, 2002, 2004), their weight is supported from above by the subducting plate, so their descent excites slab pull instead of slab suction. We thus exclude upper mantle slabs from our determination of the slab suction force so that we do not "double-count" their plate-driving contribution (Conrad and Lithgow-Bertelloni, 2002, 2004). Pieces of upper mantle slabs that are not attached to a surface plate can drive slab suction (Conrad et al., 2004). However, because the slab database (Lallemand et al., 2005) includes all tomographically-visible slabs within the slab depth parameter D, we assume here that all upper mantle slabs contribute to slab pull force.

The larger viscosity of the lower mantle allows the weight of lower mantle slabs to be supported by viscous stresses that drive global mantle flow (Conrad and Lithgow-Bertelloni, 2002, 2004). We thus drive instantaneous flow using locations and densities of slabs in the lower mantle, which were determined by advecting "slablets" into the mantle based on a plate tectonic reconstruction of rates and locations of subduction (i.e., the "slab model" Lithgow-Bertelloni and Richards, 1998; Ricard et al., 1993). We chose to drive plate motions using densities inferred from the history of subduction, rather than from seismic tomography, because plate motions driven by the slab model alone provide a better fit to observed plate motions in studies that do not include plate bending (Steiner and Conrad, 2007). Similarly, we employed a radial viscosity profile that provides the best fit to both the geoid (Lithgow-Bertelloni and Richards, 1998) and plate motions (Conrad and Lithgow-Bertelloni, 2002) in previous studies. To estimate the slab suction force, we summed the tractions that instantaneous mantle flow, determined following Lithgow-Bertelloni and Richards (1998) (also Becker and O'Connell, 2001; Conrad and Lithgow-Bertelloni, 2002, 2004), exerts on the base of each of 17 major plates (Fig. 1a). Plate boundaries for these plates were compiled by combining updated boundaries of plates defined by Bird (2003).

2.3. Plate bending force

Buffett (2006) showed that the magnitude of bending force $F_{bending}$ can be approximated by $F_{bending} = 2/3(H/R)^3 \eta_b u_0$ (Eq. (22) of Buffett, 2006), where H is plate thickness (assumed to be equal to H used for the pull force), η_b is the effective viscosity of the bending lithosphere, u_0 is the subduction convergence velocity, and R is the minimum radius of curvature of the bending slab (Fig. 1c, d), assuming that the locally-measured radius decreases continuously from infinity for the surface plate to R for the maximally-curving slab (Buffett, 2006). Here we define, as other have done (Conrad and Hager, 1999, 2001; Buffett, 2006; Buffett and Rowley, 2006; Di Giuseppe, 2008), the bending viscosity η_b as representing the effective average Newtonian viscosity that applies for the bending region of lithosphere. As a result, this parameter absorbs any variable or non-Newtonian aspects associated with the bending deformation, including brittle fracture, a possible yield stress (Billen and Hirth, 2007), or other stress-, temperature- or position-dependent variations in rheology. Note also that this parameter only applies within the bending zone; outside of this zone η_b is irrelevant. We estimated $F_{bending}$ as a function of η_b (expressed as a multiple of the upper mantle viscosity η_m) for 207 subduction zones around the world (Fig. 1a) using Eq. (22) of Buffett (2006), estimates for H and u_0 given by Lallemand et al. (2005), and new measurements of the radius of curvature R determined (e.g., Fig. 1d) by Heuret (2005) as discussed below.

Table 1
Subduction zone transect data used in this study to calculate $F_{bending}$ and F_{pull}

Transect name[a]	Trench location[a]		Subducting azimuth[a]	Segment width[a]	Radius of curvature[b]	Slab depth[a]	Subduction age[a]	Upper/lower[a]	Subducting velocity[d]
	Latitude	Longitude	(°)	(km)	R (km)	D (km)	A_S (Myr)	Plate[c]	u_0 (mm/yr)
ANDA6	14	92.1	112	236.7	340	600	85.5	17/9	2
ANDA5	12	91.6	101	225.8	350	600	82	17/9	11.8
ANDA4	10	91.4	97	225.8	360	600	77.8	17/9	8.1
ANDA3	8	91.7	77	230.2	380	670	73.7	17/9	14.2
ANDA2	6	92.6	70	205.7	400	670	69.2	17/9	22.9
ANDA1	4	93	60.8	226.6	530	670	61.1	17/9	20.4
SUM6	2	95	25	366.8	530	1200	51.8	17/4	38.6
SUM5	0	97	56	314.5	540	1200	46.2	17/4	25.2
SUM4	−2	98.1	47.3	265.2	540	1200	47.1	17/4	31.8
SUM3	−4	99.7	50	290.3	550	1200	60	17/4	33.7
SUM2	−5.5	100.8	50.8	239.4	580	1200	69	17/4	34.9
SUM1	−7	102.3	33.5	348.9	600	1200	72	17/4	46.3
JAVA7	−8.4	105	32.4	228.2	540	1200	75	17/4	49.2
JAVA6	−9.7	107	24.7	219	540	1200	78	17/4	55.1
JAVA5	−10.5	109	10	198.3	540	1200	80	17/4	59
JAVA4	−10.4	111	10	222.1	530	1200	81	17/4	60.9
JAVA3	−10.7	113	8	219.3	520	1200	82	17/4	62
JAVA2	−11.2	115	11.4	199.7	500	1200	83	17/4	63.8
JAVA1	−11.3	117	358.7	196.6	480	1200	84	17/4	65.8
TIM1	−11.1	119	9	219.3	460	670	141	17/4	39.1
TIM2	−12.1	121	1	220.9	600	670	−9999	17/4	31.3
TIM3	−11.2	123	345	232.2	500	670	−9999	17/4	25.3
TIM4	−10.2/4	125	338	232.9	360	670	−9999	17/4	25.1
TIM5	−9.6	126.5	340	222.7	260	670	−9999	17/4	25.4
TAN1	−9.2	128.5	342	222.9	260	500	−9999	17/4	9.6
TAN2	−8.7	130.5	335	223.2	400	500	−9999	17/4	6.3
TAN3	−7.1	132.5	290	343.3	500	500	−9999	17/4	0.4
TAN4	−5	133.8	269	222.3	−9999	500	−9999	17/4	14.2
SER1	−3.4	132	220	314	−9999	500	−9999	17/5	49.8
SER2	−2.7	130	188	225.5	−9999	500	−9999	17/5	11.2
SER3	−2.4	128	176	222.2	−9999	500	−9999	17/5	3
TOLO[e]	−3.5	123.8	262	225.8	−9999	−9999	10	−/−	103.9
HALM2	0	126.8	97	225.8	−9999	400	40	14/17	18.6
HALM1	2	127.3	117	314.5	−9999	400	40	14/17	0.8
SANG3[e]	1	126.4	298	290.3	−9999	670	40	−/−	75.6
SANG2[e]	3	127	281	230.2	−9999	670	40	−/−	59.8
SANG1[e]	5	126.6	268	223.2	−9999	670	40	−/−	58.7
SULA2[e]	2	123	170	230.2	200	150	40	−/−	35
SULA1[e]	2.3	121	190	225.8	−9999	150	40	−/−	25.7
SULU2[e]	7.5	121.6	124	314.5	−9999	100	20	−/−	32.5
SULU1[e]	6.5	119.7	128	346	−9999	300	20	−/−	27.2
COTO[e]	4.5	125.2	88	223.2	−9999	−9999	40	−/−	32.2
NEG4[e]	6.5	123.8	53	290.3	−9999	−9999	20	−/−	16.6
NEG3[e]	8	123.5	60	290.3	−9999	−9999	20	−/−	22.2
NEG2[e]	10	121.7	92	225.8	−9999	300	20	−/−	16.8
NEG1[e]	12	121.3	65	314.5	−9999	−9999	20	−/−	8
LUZ4[e]	14	119.2	65	290.3	190	400	22	−/−	44.8
LUZ3	16	119.2	95	230.2	200	670	18	14/17	74.3
LUZ2	17.5	119.2	88	222.4	310	670	27	14/17	89.9
LUZ1	19	119.8	119	271.5	280	670	32	14/17	95.6
BAT2	20.5	120.2	74	256.8	220	670	35	14/17	71.8
BAT1	22.5	119.9	112	256.8	−9999	670	35	14/17	93.1
TAIW	24	120.5	112	256.8	−9999	670	−9999	14/17	91.6
PHIL7	4	128.6	246	245.4	160	250	50	17/14	15.5
PHIL6	6	127.4	247.3	217.9	170	250	50	17/14	18.3
PHIL5	8	127.3	267	223.2	180	250	50	17/14	29.5
PHIL4	10	126.8	252.8	206.7	180	250	50	17/14	30.3
PHIL3	12	126.2	247.4	216.2	200	250	50	17/14	45.7
PHIL2	14	125.2	248	236.7	240	150	45	17/14	58.8
PHIL1	15.6	123.5	205	236.7	240	100	40	17/14	43.7
RYUS	23.4	124	345	204.2	340	450	35	8/14	94.2
RYUN1	24.2	127	325	247.6	380	450	38	8/14	86
RYUN2	25.7	129	320	231.4	400	350	48	8/14	87.3
RYUN3	27.5	130.5	310	257.6	360	325	50	8/14	81
RYUN4	29.8	132	300	251.9	300	300	50	8/14	78.8
NAN3	31.8	134	335	208.5	800	100	17	8/14	46.9
NAN2	32.6	135.5	340	199.3	750	100	17	8/14	41.8
NAN1	33.1	137	345	189.2	750	100	21	8/14	37.1
SUR	34.7	140	10	192.6	−9999	100	−9999	8/14	17.7
PAL	6.8	134.5	315	312.3	−9999	350	−9999	14/13	0.9
YAP3	7.3	136	358	220.6	−9999	100	35	14/13	2.5
YAP2	8.6	138	305	342.1	−9999	100	30	14/13	3.3
YAP1	10	138.6	290	256.8	−9999	100	35	14/13	2.9

Table 1 (continued)

Transect name[a]	Trench location[a]		Subducting azimuth[a]	Segment width[a]	Radius of curvature[b]	Slab depth[a]	Subduction age[a]	Upper/lower[a]	Subducting velocity[d]
	Latitude	Longitude	(°)	(km)	R (km)	D (km)	A_S (Myr)	Plate[c]	u_0 (mm/yr)
SMAR5	10.8	140.5	359	219.2	180	350	155	14/13	8.2
SMAR4	11.4	142.5	350.3	200.3	200	400	155	14/13	15
SMAR3	12	144.5	335.9	212.9	220	500	156	14/13	55.1
SMAR2	13.3	146.5	314.4	291	270	900	156.3	14/13	66
SMAR1	15	147.5	289.2	211.8	280	900	153.2	14/13	69.7
NMAR4	17	147.8	271	222.4	280	900	149.6	14/13	62.5
NMAR3	19	147.6	260	236.7	280	900	147.5	14/13	41.2
NMAR2	21	146.9	235	314.5	300	900	146.6	14/13	27.2
NMAR1	23	145.1	225.3	253.3	280	900	145.3	14/13	17.8
IZU5	25	143.2	264	225.8	260	670	150	14/13	43.4
IZU4	27	143.3	272	222.4	320	670	148	14/13	49
IZU3	29	142.9	252.3	210.4	340	670	141	14/13	44.9
IZU2	31	142.3	258	205.3	360	670	135	14/13	51.2
IZU1	33	142.1	260.9	202.3	400	670	129	14/13	55
JAP4	35	142.2	297.1	217.9	500	670	127	8/13	92.5
JAP3	37	143.5	298.9	226.8	560	670	132	8/13	91.6
JAP2	39	144.2	276.6	200.3	580	670	131	8/13	85.9
JAP1	40.5	144.5	291.9	216.5	580	670	128	8/13	90.2
SKOUR5	41.5	145.5	318.5	207.3	500	670	128	11/13	76.7
SKOUR4	42.2	147	324	191.2	420	670	120	11/13	73.5
SKOUR3	43.5	149	318.9	191.1	410	670	118	11/13	77
SKOUR2	44.4	151	329.4	163.9	380	670	118	11/13	70.8
SKOUR1	45.3	153	318.3	195.2	360	670	118	11/13	77.5
NKOUR3	47	155.1	307.6	251.2	360	900	110	11/13	79.4
NKOUR2	49	157.5	313.9	282.5	360	850	110	11/13	78
NKOUR1	51	160.2	304.1	237.9	360	850	110	11/13	76.8
KAM2	53	162.3	300	222.4	360	670	100	11/13	74.9
KAM1	54.5	163.6	300	256.8	340	400	100	11/13	73.8
W_ALE1	51.6	173	27.9	137.8	210	300	45	11/13	21.9
W_ALE2	51.1	175	16.2	130.3	220	300	45	11/13	36.1
C_ALE1	50.8	177	20.9	137.7	240	350	54	11/13	25.4
C_ALE2	50.4	179	11.6	129.6	270	400	56	11/13	41.1
C_ALE3	50.3	181	350.9	144.3	270	475	58	11/13	52
C_ALE4	50.4	183	350.2	128.8	270	550	58	11/13	60.2
C_ALE5	50.5	185	352	129.4	280	550	58	11/13	61.4
C_ALE6	50.9	187	353	127.6	280	500	63	11/13	59.5
E_ALE1	51.1	189	342.3	130.6	290	500	63	11/13	65.3
E_ALE2	51.5	191	336.2	133	310	450	61	11/13	65.7
E_ALE3	52	193	337.9	132.3	310	450	59	11/13	64.9
E_ALE4	52.5	195	338	132.5	260	400	58	11/13	64.3
E_ALE5	53.1	197	339.5	128.4	300	400	53	11/13	63.1
W_ALA1	53.5	199	343.5	124.5	400	400	52	11/13	61.4
W_ALA2	53.8	201	341.6	124	400	400	52	11/13	60.5
W_ALA3	54.2	203	341.3	123.5	520	300	52	11/13	59.4
W_ALA4	54.8	205	323.1	138.9	550	300	52	11/13	58
W_ALA5	55.6	207	330.1	127.1	600	300	49	11/13	58
E_ALA1	56.2	209	331	123.7	660	300	46	11/13	56.6
E_ALA2	57.1	211	319.6	146.1	880	300	45	11/13	51.4
E_ALA3	58	213	314.5	150.6	930	300	40	11/13	48
E_ALA4	59.1	214.5	310.6	159	1120	200	39	11/13	42.9
E_ALA5	59.2	215.5	345	117.9	1200	200	39	11/13	52
CASC1	50	231.7	70	256.8	500	400	5	11/10	43.8
CASC2	48	233.4	70	245.4	840	300	10	11/10	36.2
CASC3	46	234.1	80	225.8	−9999	300	11	11/10	30.3
CASC4	44	234.6	89	223.2	−9999	300	11	11/10	24.3
CASC5	42	234.7	86	222.4	960	300	10	11/10	26.6
MEX1	19.1	254.5	54.9	328.2	280	300	8	11/7	39.7
MEX2	17.9	256	37.4	232.7	310	300	8	11/7	47.5
MEX3	16.9	258	25	212.8	440	300	15	11/7	51.5
MEX4	16.3	260	30.4	204.9	340	300	15	11/7	55.7
MEX5	15.6	262	17.8	202.1	400	300	15	11/7	59.5
MEX6	15.3	264	9.7	196.5	440	300	15	11/7	60.6
COST1	14.2	266	21	225.4	340	300	18	6/7	63.6
COST2	13.2	268	26.5	219.5	280	400	22	6/7	68.6
COST3	12.3	270	22.2	211.1	260	400	24	6/7	73
COST4	11.4	272	32	233.8	240	400	28	6/7	77.6
COST5	9.4	274	30	219.4	260	400	26	6/7	83.6
COST6	8.4	276	29	220	540	100	16	6/7	77.6
COL1	5	281.9	113	256.8	380	670	19	15/12	42.3
COL2	3.5	280.9	120	314.5	400	670	15	15/12	46.6
COL3	2	279.9	115	290.3	420	670	12	15/12	41.3
COL4	0	279	107	245.4	500	670	15	15/12	39.2
COL5	−2	278.5	102	230.2	520	670	16	15/12	36
PER1	−4	278.1	91	200.5	520	1200	30	15/12	69.1

Table 1 (continued)

| Transect name[a]	Trench location[a]		Subducting azimuth[a]	Segment width[a]	Radius of curvature[b]	Slab depth[a]	Subduction age[a]	Upper/lower[a]	Subducting velocity[d]
	Latitude	Longitude	(°)	(km)	R (km)	D (km)	A_S (Myr)	Plate[c]	u_0 (mm/yr)
PER2	−5.5	278.1	82.9	200	520	1200	30	15/12	70.9
PER3	−7	278.4	71.4	208.2	520	1200	31	15/12	70.7
PER4	−9	279.2	64	224.2	540	1200	31	15/12	70.2
PER5	−11	280.4	58.9	233.3	490	1200	46	15/12	69.3
PER6	−13	281.7	55.5	248.4	400	1200	46	15/12	68.6
PER7	−15	283.4	50	222.4	340	1200	46	15/12	66.6
NCHI1	−17	285.9	37.8	330.9	360	1200	52	15/12	58.1
NCHI2	−19	288	56.4	240	520	1200	54	15/12	63.5
NCHI3	−21	288.7	84.4	201	620	1100	55	15/12	72.2
NCHI4	−23	288.7	94.7	201.2	700	1000	54	15/12	71.3
NCHI5	−25	288.6	93.3	201.5	700	900	53	15/12	70.8
NCHI6	−27	288.3	101.1	201.2	400	800	52	15/12	68.5
JUAN1	−29	287.7	99.4	204.5	300	670	49	15/12	68.7
JUAN2	−30.5	287.5	94.3	198.4	240	670	48	15/12	70.8
JUAN3	−32	287.4	94.8	202.2	280	670	48	15/12	70.6
SCHI1	−34	286.9	113.3	220	440	670	42	15/12	65.6
SCHI2	−35.5	286.2	118.4	219.8	500	−9999	39	15/12	61.6
SCHI3	−37	285.4	105	208.7	550	−9999	35	15/12	72.6
SCHI4	−39	284.9	99	230.2	540	−9999	33	15/12	75.5
SCHI5	−41	284.7	97	222.4	450	−9999	20	15/12	76.2
TRI1	−43	284.5	95	222.4	410	−9999	12	15/12	76
TRI2	−45	283.9	95	222.4	−9999	−9999	5	15/12	76.1
TRI3	−47	283.8	98	223.2	−9999	−9999	10	15/2	20.8
TRI4	−49	282.8	98	222.4	−9999	−9999	18	15/2	20.9
PAT1	−51	283.3	80	236.7	−9999	−9999	18	15/2	19.3
PAT2	−53	283.9	89	230.2	−9999	−9999	20	15/2	18.8
PAT3	−55	285.7	46	314.5	−9999	−9999	20	15/2	12
BARB1	12	302.6	278	225.8	580	670	117	6/15	12.7
BARB2	14	302.3	251	223.2	460	670	110	6/15	11.9
ANTI1	16	301.2	250	230.2	450	670	98	6/11	10.8
ANTI2	18	299.8	230	314.5	420	670	90	6/11	9.6
ANTI3	19.3	298	205	223.4	400	500	84	6/11	5.9
PORTO1	19.8	296	185	210	300	500	92	6/11	8.1
PORTO2	19.8	294	176	210	230	500	100	6/11	7.2
PORTO3	19.7	292	176	209.4	180	500	110	6/11	7.2
FRAN	20	290	194	216.4	−9999	500	117	6/11	2.6
SAND1	−60	335.4	319	271.5	240	670	33	16/15	35.7
SAND2	−58	336.2	265	223.2	240	670	36	16/15	78
SAND3	−56	334.9	240	290.3	220	670	40	16/15	72.4
SAND4	−55.1	333	205	140.2	160	670	40	16/15	35.1
SAND5	−54.9	331	184	128.3	160	−9999	40	16/15	15.1
SAND6	−54.8	329	190	132.8	−9999	−9999	40	16/15	3.6
PUY	−48	164.5	98	271.5	−9999	150	33	13/4	23.8
HIKS1	−42.3	175	320	314.5	320	670	−9999	4/13	17.7
HIKS2	−41.4	177	332	314.5	480	670	−9999	4/13	13.3
HIKS3	−40	178.7	287	225.8	460	670	−9999	4/13	38
HIKN1	−38.5	179.1	288	225.8	310	670	−9999	4/13	40.8
HIKN2	−36.5	180.6	292	230.2	280	670	−9999	4/13	43.8
KER1	−35	181.6	292.5	200.5	260	900	95	4/13	46.6
KER2	−33	182.2	287.9	206.4	220	1000	97	4/13	51.4
KER3	−31	183.2	291.1	213.9	260	1100	99	4/13	54.3
KER4	−29	183.9	286.4	212	270	1200	101	4/13	59.6
KER5	−27	184.5	281.2	201.9	280	1300	103	4/13	64.1
TONG1	−25	184.8	275.9	202.4	280	670	105	4/13	71.2
TONG2	−23	185.4	297.9	227.2	300	670	106	4/13	103.9
TONG3	−21	186.5	291.1	215.8	300	670	107	4/13	153
TONG4	−19	187.2	286.8	208.3	300	670	108	4/13	182.1
TONG5	−17	187.8	286.1	204.4	320	670	108	4/13	205.4
TONG6	−15.5	187.7	241.4	221.9	−9999	670	109	4/13	223.2
SHEB1	−22	169.5	44.6	291.5	160	500	−9999	13/4	71.4
SHEB2	−20	168.2	61.4	224.2	160	670	45	13/4	118.6
SHEB3	−18	167.4	81.5	200.4	160	670	48	13/4	99.3
ENTR	−16	166.6	64	256.8	180	670	56	13/4	38.3
NHEB1	−14	166.2	83	230.2	140	670	60	13/4	107.6
NHEB2	−12	165.7	66	283.8	120	670	60	13/4	165.5
SALOM4	−11	164	352	240.9	−9999	500	−9999	13/4	141
SALOM3	−11.3	162	5	241	−9999	670	−9999	13/4	27
SALOM2	−10.3	160	22	241.3	−9999	670	31	13/4	55.1
SALOM1	−9.3	158	29	242.2	−9999	500	31	13/4	65.7
BOUG2	−8	156	33	254.4	130	500	31	13/4	102.3
BOUG1	−6.5	154	35	255.2	140	670	31	13/4	93.8
BRET3	−6.1	152	335	235.3	180	670	31	13/4	120
BRET2	−7	150	339	243.6	260	670	31	13/4	75.2
BRET1	−7.3	148	10	202.6	220	670	31	13/4	64
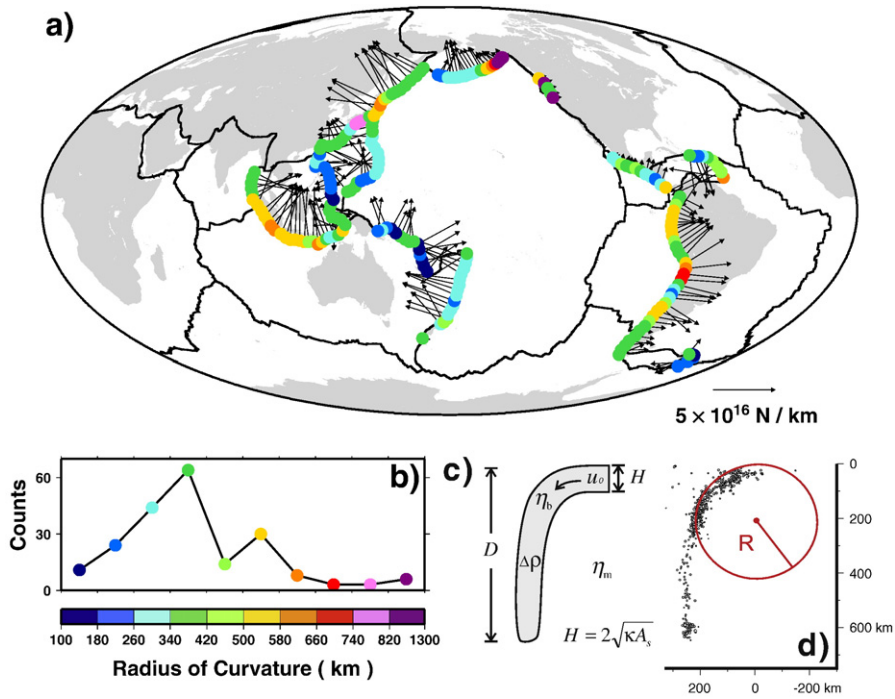
Fig. 1. Slab pull forces (a, direction and magnitude given by arrows) and radius of curvature (a, colored dots) for each of the 207 subduction zones defined by Lallemand et al. (2005) and Heuret (2005) that were used in this study (Table 1). Pull forces were determined using estimates of the parameters defined in (c) and given by (Lallemand et al. (2005)); measured values of R, which are distributed as in (b), were determined for the maximally-curving part of the slab, as described in the text and exemplified for a Marianas profile in (d). (For interpretation of the references to color in this figure legend, the reader is referred to the web version of this article.)

2.4. Measurement of the slab radius of curvature

Heuret (2005) measured the radius of curvature for bending at each of the subduction zones defined by Heuret and Lallemand (2005) (Table 1, Fig. 1a). For each subduction profile, this was accomplished by plotting the slab hypocenters of Engdahl et al. (1998) between the surface and about 150 km depth beneath a series of concentric circles positioned so that one of them corresponds to the best-fitting envelope for the upper boundary of the Wadati–Benioff zone (Fig. 1d). The angle of the circle that is used to fit the observed seismicity ranges from about 25° for "flat slab" geometries (shallow dip) to nearly 90° for the most steeply-dipping subduction zones. For the flattest slabs, the zone of seismicity is limited by the termination of seismicity beneath about 150 km depth. These locally-measured values of R typically depend on where along the descending slab that R is measured; R may vary between infinity (for both the flat surface plate and the deep descending slab) and a minimum value for the maximally-curving part of the slab. For the purposes of this work, we used the minimum value of R, which is what Buffett (2006) used to estimate the plate bending force in their Eq. (22). Uncertainty in the measurement of R, estimated based on the relative fits of neighboring concentric circles to the seismicity, ranges from about ±10 km for $R \sim 120$ km to about ±50 km for $R \sim 600$ km. The radius of curvature also correlates with the subtending angle used to constrain R. This angle ranges from 25° for $R > \sim 800$ km to 90° for $R < \sim 250$ km, and varies approximately linearly between these values for 250 km $< R <$ 800 km.

Uncertainty is higher for slabs that bend twice (such as those beneath South America); in this case we chose the first bending, which typically features a smaller value of R.

The radii measured by Heuret (2005) (Fig. 1a) range from about 100 to 1200 km (Fig. 1b), with the largest values corresponding to the shallow-dipping slabs. Most (~90%) of the slabs have radii between 120 and 600 km, with a mean value of 390 km and a standard deviation of about 190 km (Fig. 1b). We note that significant variability in R has also been demonstrated previously in laboratory experiments (Bellahsen et al., 2005). Our estimate of the mean value of $R = 390$ km for the earth is significantly larger than the previous estimate of 200 km made by Bevis (1986), which was based on a fit to a single Wadati–Benioff zone profile for the Marianas that was taken from Isacks and Barazangi (1977). In fact, prior to this study, the Isacks and Barazangi (1977) study, which displays seismicity profiles for 12 subduction zone transects, was the most complete global analysis of patterns of slab bending to date. The 12 profiles of Isacks and Barazangi (1977) show variability in slab curvature, so it is perhaps not surprising that we observe variability in the curvature measurements in this study. Nevertheless, the Bevis (1986) estimate of $R = 200$ km has been used in most previous attempts to apply plate bending models to subduction zones (Conrad and Hager, 1999, 2001; Buffett, 2006; Buffett and Rowley, 2006). Our observation that the average value of R should be approximately double the value used in previous studies will cause F_{bending} to decrease, on average, by a factor of eight, for a given value of η_{b}.

Notes to Table 1:

−9999 indicates insufficient data to acquire a proper estimate. For these cases, we assume $A_S = 50$ Myr, $D = 670$ km, or $R = 390$ km (average value).

[a] Transect data from Lallemand et al. (2005).

[b] Radius of curvature data from Heuret (2005).

[c] Numbers correspond to plate names: 1 = Africa, 2 = Antarctica, 3 = Arabia, 4 = Australia, 5 = Bird's head, 6 = Caribbean, 7 = Cocos, 8 = Eurasia, 9 = India, 10 = Juan de Fuca, 11 = North America, 12 = Nazca, 13 = Pacific, 14 = Philippine Sea, 15 = South America, 16 = Scotia, 17 = Sunda.

[d] Subducting velocity u_0 is taken to be the relative motion between the trench and the subduction plate (determined from $V_{\mathrm{tn}} + V_{\mathrm{subn}}$ from Lallemand et al. (2005)).

[e] Indicates transect not used in the analysis because the subducting plate is too small to be included in our analysis.

3. Constraints from observed plate motions

Plate-driving torques such as slab pull or slab suction must exactly balance the resisting torques associated with the motion of the plates over the mantle (mantle drag), as well as the bending deformation at subduction zones. Mantle drag can be computed by moving each plate individually in each Cartesian direction; this information can be used to invert for the set of plate motions that exactly balances resisting forces with the driving forces in a no-net-torque reference frame (Ricard and Vigny, 1989). We subtract our estimates of $F_{bending}$ from those of F_{pull} (Fig. 1a) and $F_{suction}$ to predict plate motions for different values of the bending viscosity η_b. We then used the observed relative plate motions (Fig. 2a) to constrain η_b.

We compare predicted and observed plate motions in the no-net-rotation reference frame because the amount of observed net rotation is poorly constrained, and may be the result of plate-mantle coupling that is not included here (e.g., Becker, 2006). Predicted and observed velocity fields are quantitatively compared using the misfit function defined by Steiner and Conrad (2007). This function expresses the area-weighted average magnitude (on a 1° by 1° grid) of the vector difference between predicted and observed plate motion vectors. Predicted velocities are scaled so that their average speed is equal to that of observed plate motions, which is permissible because the absolute mantle viscosity, which controls plate speeds, is uncertain by at least a factor of 3. Thus, the misfit function is sensitive to the direction of plate motions as well as differences between the relative speeds of different plates (Steiner and Conrad, 2007). For a weakly bending slab ($\eta_b = \eta_m$), predicted plate motions (Fig. 2b) qualitatively match those that Steiner and Conrad (2007) computed using similar models that do not include bending. The slight difference in the misfit

parameter (0.46 for this study vs. 0.39 for Steiner and Conrad, 2007) results from differences in the definition of the pull force, and in the choice of plate boundaries. For example, the plate boundaries used here were determined from Bird (2003) so that the Lallemand et al. (2005) trench locations of subduction zone transects fall exactly on a plate boundary. In addition, our calculation of F_{pull} is determined from the Lallemand et al. (2005) data, rather than the upper mantle component of the mantle slab heterogeneity model (Lithgow-Bertelloni and Richards, 1998) that was used by Steiner and Conrad (2007).

If $\eta_b = \eta_m$ (i.e. no lithospheric strengthening in the bending region), then the bending force, $F_{bending}$, is less than 5% of the pull force everywhere (Fig. 2b, circles), meaning that nearly the entire weight of upper mantle slabs participates in slab pull. This set of forces produces a set of predicted plate motions (Fig. 2b, arrows) that, to first order, fits observed plate motions (Conrad and Lithgow-Bertelloni, 2004) (Fig. 2a). When the lithosphere viscosity η_b is increased to $100\eta_m$ and then $1000\eta_m$, the bending resistance becomes increasingly important for the global force balance (colored circles, Fig. 2c and d). The result is a slowing of subducting plates because the increased resistance to subduction diminishes the slab pull force. By contrast, overriding plates may speed up because the lack of a strong pull force allows the symmetrical slab suction force to drive them faster toward the trench (Conrad and Lithgow-Bertelloni, 2004). Because the Pacific plate has the oldest, and therefore thickest, plates, its motion is most dramatically affected by the addition of the bending force. Strong bending forces in the western Pacific resist the motion of the Pacific plate in that direction, slowing its motion relative to the other plates (Fig. 2d, arrows) by cutting off the pull force almost entirely (purple circles in the western Pacific). By contrast, the subducting Nazca plate
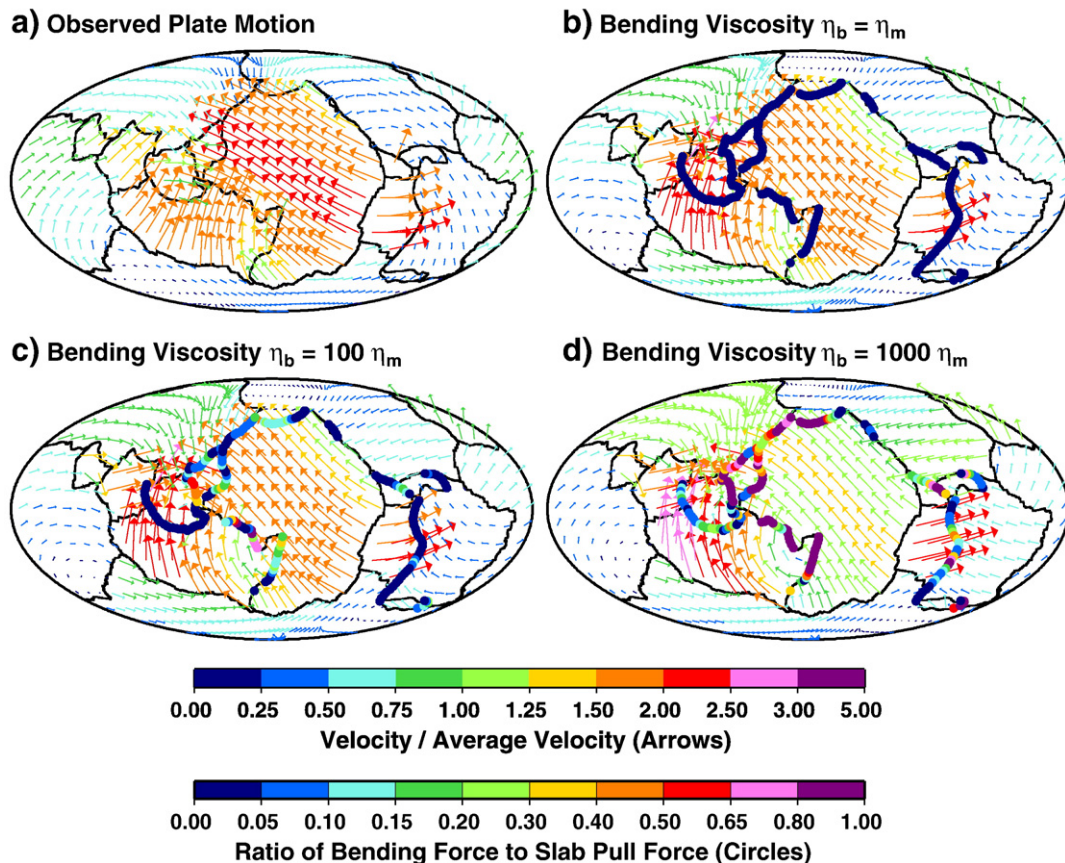

a) Observed Plate Motion

b) Bending Viscosity $\eta_b = \eta_m$

c) Bending Viscosity $\eta_b = 100\ \eta_m$

d) Bending Viscosity $\eta_b = 1000\ \eta_m$

| 0.00 | 0.25 | 0.50 | 0.75 | 1.00 | 1.25 | 1.50 | 2.00 | 2.50 | 3.00 | 5.00 |

Velocity / Average Velocity (Arrows)

| 0.00 | 0.05 | 0.10 | 0.15 | 0.20 | 0.30 | 0.40 | 0.50 | 0.65 | 0.80 | 1.00 |

Ratio of Bending Force to Slab Pull Force (Circles)

Fig. 2. Comparisons of (a) observed plate motions (Bird, 2003) in a no-net-rotation reference frame with (b, c, d) predictions based on bending viscosities η_b equal to η_m, $100\eta_m$, and $1000\eta_m$, respectively. The length and color of arrows indicate the magnitude of plate velocity. Colored circles represent the ratio of the bending force, $F_{bending}$, to the slab pull force, F_{pull}. (For interpretation of the references to color in this figure legend, the reader is referred to the web version of this article.)

is younger than ~50 My when it subducts, and thus produces thinner slabs that are not dramatically affected by bending. Although slowed slightly when $\eta_b = 1000\eta_m$, the Nazca plate's motion remains fairly constant as the plate viscosity is increased, and $F_{bending}$ is $< \sim 20\%$ of F_{pull} along most of the South American margin (Fig. 2d). Finally, increased η_b causes the Australian plate's motion to be diverted toward the Java–Bengal subduction zones of the Indonesian arc and away from the New Hebrides subduction zones to the east (Figs. 2b–d). This is because of larger R for the Indonesian subduction zones (500–600 km vs. 100–400 km for New Hebrides, Fig. 1a), which allow weaker bending and thus greater pull forces along the Indonesian arc.

Primarily because of changes in the motions of the Pacific (the largest plate, and the biggest contributor to the area-weighted misfit function) and Australian plates, we find that increased importance for bending tends to worsen the fit to plate motions (Fig. 3a). Compared to

Fig. 3. Variation of (a) misfit and (b) plate-driving forces as a function of the bending viscosity η_b relative to the upper mantle viscosity η_m. The misfit for plate motions driven by slab pull alone (blue lines) or the combination of slab pull and slab suction (red lines) is shown in (a) for both all plates (circles) and subducting plates only (triangles). The large red star shows the viscosity cutoff $\eta_b = 300\eta_m$, above which bending overly slows subducting plate motions. For all plates driven by slab pull and slab suction (red circles in a), we show in (b) the variation of the bending term relative to the slab pull force (red line) and to the total plate-driving forces (green line), as well as the net pull force relative to the plate-driving forces (blue line). (For interpretation of the references to color in this figure legend, the reader is referred to the web version of this article.)

the best-fitting case of $\eta_b = \eta_m$, a bending viscosity of $100\eta_m$ increases the misfit by 7.6%, while $\eta_b = 1000\eta_m$ increases the misfit by ~47% (red circles, Fig. 3a). Results are similar if we exclude the overriding plates and consider only the misfit for the subducting plates (red triangles, Fig. 3a). To emphasize the influence of plate bending even more directly, we exclude the slab suction force from the lower mantle entirely and drive plates using slab pull modified by plate bending (blue lines, Fig. 3a). In this case, we observe an even sharper increase in misfit because the bending resistance has a proportionally stronger influence on the net force on plates.

Because the change in misfit within the range $\eta_m < \eta_b < 100\eta_m$ is small (Fig. 3a, also compare Fig. 2b and c), we surmise that all viscosities within this range are possible. However, the misfit begins to increase more rapidly for $\eta_b > 100\eta_m$, and for $\eta_b \approx 1000\eta_m$ the misfit is intolerable (Fig. 2d). A cutoff value of $\eta_b \sim 300\eta_m$ (red star in Fig. 3a), which is between these extremes, expresses the maximum possible bending viscosity that allows an acceptable prediction of plate motions. This choice of the maximum bending viscosity, $\eta_b \approx 300\eta_m$, yields a misfit that has increased by 15% (0.07) relative to the best-fitting $\eta_b = \eta_m$ case. This misfit increase is 2/3 that of the improvement in misfit (0.11) achieved by the introduction of the slab pull force itself (Conrad and Lithgow-Bertelloni, 2002; misfit measured by Steiner and Conrad, 2007), and equivalent to the misfit produced by a South America-sized plate moving in a direction that is oriented 55° from its observed direction (Steiner and Conrad, 2007). Using this cutoff, which is approximately midway between the well-fitting case of $\eta_b = 100\eta_m$ (Fig. 2c) and the poor-fitting case of $\eta_b = 1000\eta_m$ (Fig. 2d), we infer an upper bound on the lithosphere viscosity of $\eta_b < \sim 300\eta_m$ (red star in Fig. 3a).

4. Discussion and conclusions

Our upper bound on the bending viscosity also places an upper bound on the importance of the bending deformation for global mantle flow. In particular, for $\eta_b < \sim 300\eta_m$, the bending deformation counteracts at most ~35% of the average pull force from upper mantle slabs (red line, Fig. 3b). This upper bound is close to Buffett and Rowley (2006) estimate of ~36% and ~34% for bending the old, thick slabs of the Australian (Java trench) and Pacific plates, but larger than their estimate of ~14% and ~6% for bending the younger and thinner Nazca and Cocos slabs. Thus, when compared to the pull force alone, our estimate of the bending deformation (35%) is slightly higher than the global average estimated by Buffett and Rowley (2006) (about 20–30%, which is between the groups of estimates in Buffett and Rowley, 2006). However, when compared to the net forces on plates (including slab suction), we find that the bending resistance cannot represent more than ~25% of the driving forces on plates (green line, Fig. 3b). This value is close to the global average of Buffet and Rowley (2006) (who include thermal subsidence but not slab suction or lower mantle slabs) and within the ranges given by other studies of the subduction zone flow field (Di Giuseppe et al., 2008; Capitanio et al., 2007). For the maximum bending dissipation at $\eta_b \sim 300\eta_m$, we find that the net slab pull force ($F_{pull} - F_{bending}$) accounts for ~40% of the driving forces on plates (blue line, Fig. 3b), while slab suction accounts for ~60%. By contrast, slab pull and slab suction account for ~60% and ~40% of plate-driving forces, respectively, in the absence of plate bending (Conrad and Lithgow-Bertelloni, 2004, and blue line in Fig. 3b).

Our conclusion that the bending deformation does not account for more than ~25% of the forces on plates, and not more than ~35% of the pull force, relies on the notion that slab pull from upper mantle slabs is essential for explaining global plate motions. To date, the combination of upper mantle slab pull and lower mantle slab suction (Conrad and Lithgow-Bertelloni, 2002, 2004) provides the best prediction of observed plate motions, but it does not take into account several forces that may also affect plate motions. In particular, our model does not include lateral variations in viscosity, which may affect the
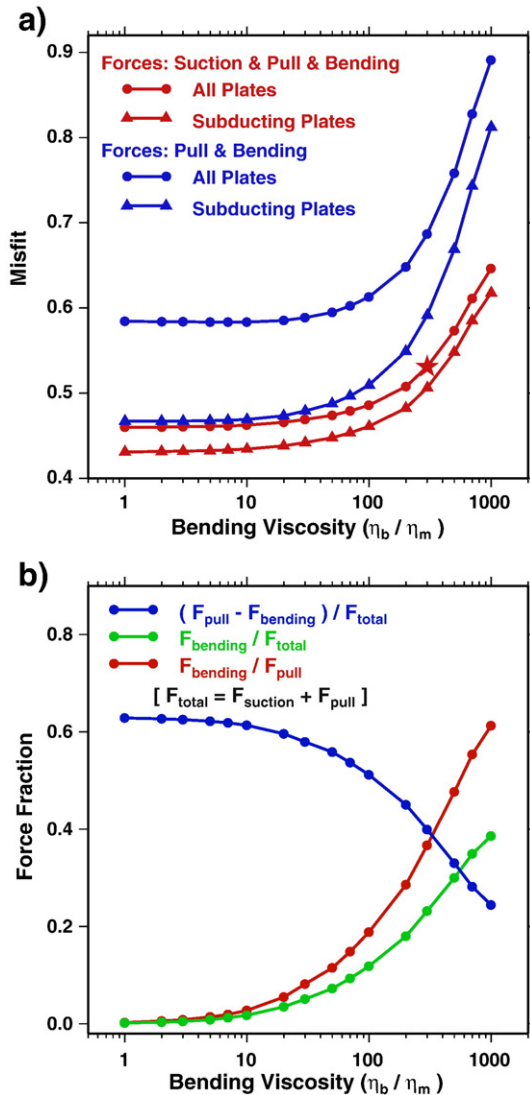
motions of continental plates (Becker, 2006; Zhong, 2001) or the effect of active mantle upwellings (Steiner and Conrad, 2007; Lithgow-Bertelloni and Silver, 1998). In addition, we note that because we do not implement a detailed model for the deformation and flow in the subduction zone, viscous flow either above the slab (corner flow), along the slab (trench-parallel flow), or around its edges (toroidal flow) could exert important tractions on the surface plates nearby. Other neglected forces, such as continent–continent collision or plate interaction across transform faults, may also affect the force balance on plates. Finally, although we have chosen mantle viscosity and density heterogeneity structures that provide the best fit to the geoid and plate motions in the absence of plate bending, it is possible that other choices for these mantle properties, possibly in conjunction with some combination of additional forces on plates, could produce a better fit if bending is included. However, none of these factors tends to preferentially speed subducting plates relative to overriding plates, which would be necessary to offset the tendency of plate bending to diminish the overall misfit.

Although the plate motion constraint on bending favors weak slabs, plate motions also require a strong pull force, which favors strong slabs. The slab pull forces of Fig. 1, when expressed within the entire slab thickness H, produce extensional stresses within the range 65–440 MPa (with an average of 350 MPa). When this pull force is diminished by the maximum possible bending resistance at $\eta_b = 300\eta_m$, the average net pull force at the surface is ~275 MPa. The net pull force should remain fairly constant throughout the bending zone because both the pull force and the bending resistance decrease with depth. For example, at ~200 km depth beneath the bending zone, the pull force is decreased by ~30% and the bending stress vanishes to produce an average net pull force of ~245 MPa. Considering $\eta_b < $ ~$300\eta_m$ and an upper mantle viscosity within the 3–6×10^{20} Pa s range (Mitrovica, 1996), our results suggest a lithosphere viscosity no larger than $\eta_b \sim 2\times10^{23}$ Pa s. Applying a stress of 275 MPa to such a slab will generate extensional strain rates of up to ~10^{-15} s^{-1} within the bending region of the slab. Strain rates of ~10^{-15} s^{-1} have been detected within the shallow portion of slabs by estimates of seismic moment accumulation rates (e.g., Bevis, 1988), and can be accommodated by stretching within a coherent viscous slab without significantly degrading slab integrity (Capitanio et al., 2007). Oceanic lithosphere undergoing strain rates of 10^{-15} s^{-1} can support differential stresses up to ~600 MPa (Kohlstedt et al., 1995), which are more than sufficient to maintain the estimated ~275 MPa maximum pulling stress on plates. However, there is no evidence for slabs straining significantly faster than 10^{-15} s^{-1}, which suggests that the effective viscosity of the bending portion of slabs cannot be significantly smaller than $\eta_b = 2\times10^{23}$ Pa s if the required pull force is to be maintained. This value is close to the upper bound of the bending constraint ($\eta_b < $ ~$300\eta_m$), and is consistent with estimates from laboratory studies ($150\eta_m < \eta_b < 500\eta_m$, Funiciello et al., in press). Although such strong slabs are not favored by some geoid studies (Moresi and Gurnis, 1996; Zhong and Davies, 1999), detailed studies that carefully treat the asymmetrical nature of subduction do a good job of matching both bathymetry and geoid in the vicinity of coherent subducting slab with effective viscosity close to our constraint (~10^{23} Pa s in Billen et al., 2003). By contrast, some recent numerical studies suggest much higher slab viscosities of 500–$2000\eta_m$ (Di Giuseppe et al., 2008) or more (Billen and Hirth, 2007).

Studies that use models of bending dissipation to constrain the bending viscosity typically require a smaller viscosity ($300\eta_m$ and 2×10^{23} Pa s in this study vs. 50–$200\eta_m$ in Conrad and Hager, 1999, and 0.6×10^{23} Pa s in Buffett and Rowley, 2006) and a similar or larger bending dissipation (~25% in this study, ~20–30% in Buffett and Rowley, 2006, and ~40% in Conrad and Hager, 1999) than we have inferred here. This discrepancy occurs because our new radius of curvature measurements (Fig. 1) feature larger average values (~390 km) that are nearly double those suggested by previous studies (~200 km, Bevis, 1986).

Because both $F_{bending}$ and the bending dissipation depend on the inverse cube of the radius of curvature (Conrad and Hager, 1999; Buffett, 2006), doubling of R decreases the importance of bending by nearly an order of magnitude. This decrease permits the high slab viscosities that are necessary to transmit the slab pull force, while avoiding the extremely high levels of energy dissipation that are associated with deforming a highly viscous plate. Since plate bending can accommodate at most only about ~40% of global energy dissipation before subduction zones lock up (Conrad and Hager, 2001), gently curving slabs, rather than a small bending viscosity, may be the factor that stabilizes plate tectonics on Earth compared to the stagnant lid convective styles of Mars and Venus (e.g., Solomatov and Moresi, 1997).

References

Becker, T.W., 2006. On the effect of temperature and strain-rate viscosity on global mantle flow net rotation, and driving forces. Geophys. J. Int. 167, 943–957.

Becker, T.W., O'Connell, R.J., 2001. Predicting plate velocities with mantle circulation models. Geochem. Geophys. Geosyst. 2 (12). doi:10.1029/2001GC000171.

Becker, T.W., Faccenna, C., O'Connell, R.J., Giardini, D., 1999. The development of slabs in the upper mantle: insights from numerical and laboratory experiments. J. Geophys. Res. 104 (B7), 15207–15226.

Bellahsen, N., Faccenna, C., Funiciello, F., 2005. Dynamics of subduction and plate motion in laboratory experiments: insights into the "plate tectonics" behavior of the Earth. J. Geophys. Res. 110, B01401. doi:10.1029/2004JB002999.

Bevis, M., 1986. The curvature of Wadati–Benioff zones and the torsional rigidity of subducting plates. Nature 323, 52–53.

Bevis, M., 1988. Seismic slip and down-dip strain rates in Wadati–Benioff zones. Science 240, 1317–1319.

Billen, M.I., Hirth, G., 2007. Rheologic controls on slab dynamics. Geochem., Geophys., Geosyst. 8, Q08012. doi:10.1029/2007GC001597.

Billen, M.I., Gurnis, M., Simons, M., 2003. Multiscale dynamics of the Tonga–Kermadec subduction zone. Geophys. J. Int. 153, 359–388.

Bird, P., 2003. An updated digital model of plate boundaries. Geochem. Geophys. Geosys. 4 (3), 1027. doi:10.1029/2001GC000252.

Buffett, B.A., 2006. Plate force due to bending at subduction zones. J. Geophys. Res. 111, B09405. doi:10.1029/2006JB004295.

Buffett, B.A., Rowley, D.B., 2006. Plate bending at subduction zones: consequences for the direction of plate motions. Earth Planet. Sci. Lett. 245 (1–2), 359–364.

Capitanio, F.A., Morra, G., Goes, S., 2007. Dynamic models of downgoing plate-buoyancy driven subduction: subduction motion and energy dissipation. Earth Planet. Sci. Lett. 262, 284–297.

Conrad, C.P., Hager, B.H., 1999. Effects of plate bending and fault strength at subduction zones on plate dynamics. J. Geophys. Res. 104, 17551–17571.

Conrad, C.P., Hager, B.H., 2001. Mantle convection with strong subduction zones. Geophysical Journal International 144 (2), 271–288.

Conrad, C.P., Lithgow-Bertelloni, C., 2002. How mantle slabs drive plate tectonics. Science 298, 207–209.

Conrad, C.P., Lithgow-Bertelloni, C., 2004. The temporal evolution of plate driving forces: importance of "slab suction" versus "slab pull" during the Cenozoic. J. Geophys. Res. 109, B10407. doi:10.1029/2004JB002991.

Conrad, C.P., Bilek, S., Lithgow-Bertelloni, C., 2004. Great earthquakes and slab pull: interaction between seismic coupling and plate-slab coupling. Earth Planet. Sci. Lett. 218, 109–122.

Di Giuseppe, E., van Hunen, J., Funiciello, F., Faccenna, C., Giardini, D., 2008. Slab stiffness control of trench motion: insights from numerical models. Geochem., Geophys. Geosyst. 9, Q02014. doi:10.1029/2007GC001776.

Elsasser, W.M., 1969. Convection and stress propagation in the upper mantle. In: Runcorn, S.K. (Ed.), The Application of Modern Physics to the Earth and Planetary Interiors. Wiley-Interscience, Hoboken, NJ, pp. 223–246.

Engdahl, R., van der Hilst, R., Buland, R., 1998. Global teleseismic earthquake relocation with improved travel times and procedures for depth determination. Bull. Seism. Soc. Amer. 88, 722–743.

Faccenna, C., Heuret, A., Funiciello, F., Lallemand, S., Becker, T.W., 2007. Predicting trench and plate motion from the dynamics of a strong slab. Earth Planet. Sci. Lett. 257, 29–36.

Funiciello, F., Faccenna, C., Heuret, A., Di Giuseppe, E., Lallemand, S., and Becker, T.W., (in press), Trench migration, net rotation, and slab — mantle coupling, Earth Planet. Sci. Lett. doi:10.1016/j.epsl.2008.04.06

Hager, B.H., O'Connell, R.J., 1981. A simple global model of plate dynamics and mantle convection. J. Geophys. Res. 86, 4843–4867.

Heuret, A., (2005), Dynamique des zones de subduction: Etude statistique globale et approche analogique, PhD thesis, Universite Montpellier II.

Heuret, A., Lallemand, S., 2005. Plate motions, slab dynamics, and back-arc deformation. Phys. Earth Planet. Int. 149, 321–336.

Isacks, B.L., Barazangi, M., 1977. Geometry of Benioff zones: lateral segmentation and downwards bending of the subducted lithosphere. In: Talwani, M., Pitman, W. (Eds.), Island Arcs, Deep Sea Trenches and Back-Arc Basins. Am. Geophys. Union, Washington, DC, pp. 99–114.

Kohlstedt, D.L., Evans, B., Mackwell, S.J., 1995. Strength of the lithosphere: constraints imposed by laboratory experiments. J. Geophys. Res. 100 (B9), 17587–17602.

Lallemand, S., Heuret, A., Boutelier, D., 2005. On the relationships between slab dip, back-arc stress, upper plate absolute motion, and crustal nature in subduction zones. Geochem. Geophys. Geosyst. 6, Q09006. doi:10.1029/2005GC000917.

Lithgow-Bertelloni, C., Richards, M.A., 1998. The dynamics of Cenozoic and Mesozoic plate motions. Rev. Geophys. 36 (1), 27–78.

Lithgow-Bertelloni, C., Silver, P.G., 1998. Dynamic topography, plate driving forces, and the African Superswell. Nature 395, 269–272.

Mitrovica, J.X., 1996. Haskell [1935] revisited. J. Geophys. Res. 101, 555–569.

Moresi, L., Gurnis, M., 1996. Constraints on the lateral strength of slabs from three-dimensional dynamic flow models. Earth Planet. Sci. Lett. 138, 15–28.

Ricard, Y., Vigny, C., 1989. Mantle dynamics and induced plate tectonics. J. Geophys. Res. 94, 17543–17559.

Ricard, Y., Richards, M.A., Lithgow-Bertelloni, C., le Stunff, Y., 1993. A geodynamical model of mantle density heterogeneity. J. Geophys. Res. 98, 21895–21909.

Richter, F.M., 1977. On the driving mechanism of plate tectonics. Tectonophysics 38, 61–88.

Solomatov, V., Moresi, L.N., 1997. Three regimes of mantle convection with non-Newtonian viscosity and stagnant lid convection on the terrestrial planets. Geophys. Res. Lett. 24, 1907–1910.

Stein, C.A., Stein, S., 1992. A model for the global variation in oceanic depth and heat flow with lithospheric age. Nature 359, 123–129.

Steiner, S.A., Conrad, C.P., 2007. Does active mantle upwelling help drive plate motions? Phys. Earth Planet. Int. 161, 103–114.

Zhong, S., 2001. Role of ocean–continent contrast and continental keels on plate motion, net rotation of lithosphere and the geoid. J. Geophys. Res. 106, 703–712.

Zhong, S., Davies, G.F., 1999. Effects of plate and slab viscosities on the geoid. Earth Planet. Sci. Lett. 170, 487–496.